Tissue Variability and Antennas for Power Transfer to Wireless Implantable Medical Devices

**KARA N. BOCAN, (Student Member, IEEE), MARLIN H. MICKLE, (Life Fellow, IEEE),
AND ERVIN SEJDIĆ, (Senior Member, IEEE)**

Department of Electrical and Computer Engineering, University of Pittsburgh, Pittsburgh, PA 15260, USA

CORRESPONDING AUTHOR: E. SEJDIĆ (esejdic@ieee.org)

ABSTRACT The design of effective transcutaneous systems demands the consideration of inevitable variations in tissue characteristics, which vary across body areas, among individuals, and over time. The purpose of this paper was to design and evaluate several printed antenna topologies for ultrahigh frequency (UHF) transcutaneous power transfer to implantable medical devices, and to investigate the effects of variations in tissue properties on dipole and loop topologies. Here, we show that a loop antenna topology provides the greatest achievable gain with the smallest implanted antenna, while a dipole system provides higher impedance for conjugate matching and the ability to increase gain with a larger external antenna. In comparison to the dipole system, the loop system exhibits greater sensitivity to changes in tissue structure and properties in terms of power gain, but provides higher gain when the separation is on the order of the smaller antenna dimension. The dipole system was shown to provide higher gain than the loop system at greater implant depths for the same implanted antenna area, and was less sensitive to variations in tissue properties and structure in terms of power gain at all investigated implant depths. The results show the potential of easily-fabricated, low-cost printed antenna topologies for UHF transcutaneous power, and the importance of environmental considerations in choosing the antenna topology.

INDEX TERMS Wireless power transfer, implantable medical devices, tissue dielectric properties, transcutaneous energy transfer, antennas.

I. INTRODUCTION

Passive wireless implantable medical devices provide opportunities for improved patient monitoring, documentation, and treatment. Powered transcutaneously by electromagnetic waves, passive implantable devices enable miniature, battery-less implants, but consequently depend on reliable power transfer through tissue. Passive wireless implantable devices have no implanted battery, instead harvesting energy from incident electromagnetic waves, allowing dramatic miniaturization and extended lifetime of the implant [1]–[4]. Additionally, passive devices are particularly well-suited for periodic monitoring in combination with implanted biosensors, which only need to be powered when obtaining a sensor reading [5], [6]. The function of passive implantable devices is dependent on the generation of electromagnetic fields at the implantation site and the efficient capture of energy using implantable antennas.

A practical transcutaneous system must be expected to function reliably for each patient and across various patients. However, biological tissue is a variable and often unpredictable medium for electromagnetic power transmission [7]. Depending on the application, a transcutaneous system may need to function at different locations in the body where there are differences in tissue structure (e.g., reading from implanted biosensors at various body locations). For example, skin and fat will be encountered for subcutaneous implants in the leg and the arm, while power transfer through the skull must be considered for cortical implants. Even the same body area is expected to have different composition among individuals, due to variations in characteristics such as body fat content and muscle size [8]. Tissue properties also vary within a single individual over time due to changes in body fat and fluid content with age or behavior [9]–[11]. All such tissue variations affect electromagnetic power

transfer to a passive implantable device and therefore dictate the functionality of a wireless transcutaneous system.

While previous studies have investigated the effect of tissue and tissue variations on implantable antenna properties including input impedance, they are mostly dedicated to examining the implantable antenna alone or they focus on a single antenna topology (typically loop antennas) [12]–[20]. In transcutaneous systems where the external antenna is in proximity to the implant, the external and implanted antenna are not isolated. IEEE Standard C95.1 defines the far field region boundary as $2D^2/\lambda$, where D is the antenna dimension and λ is the electromagnetic wavelength [21]. The field region and power transfer mechanisms of an antenna system are therefore dependent on the operating frequency, the antenna dimensions, the transmission medium, and the antenna separation distance.

When the two antennas are not isolated, they must be analyzed simultaneously to account for loading effects of the implant in addition to effects of the tissue medium [16], [17], [20]. Mark *et al.* performed such a two-antenna analysis, investigating variability and uncertainty in thickness and dielectric properties of tissues in the head, determining the maximum achievable gain across a frequency range of 100 MHz to several GHz using loop antennas [17]. However, maximum achievable gain assumes simultaneous conjugate matching to maximize power transfer, while the power gain of a two-antenna system is ultimately sensitive to mismatch due to changes in the system impedance [22]. It is therefore important to quantify the effects of tissue variability on a transcutaneous system, to ensure the system continues to function efficiently and safely in variable tissue environments.

The goals of this study were to compare antenna topologies in terms of transcutaneous power gain and to examine the effects of tissue variability. The choice of antenna topology is integral to the function of a system, and the optimal choice of topology can improve power transfer while also simplifying the design of impedance matching networks.

In the first part of this work, four printed antenna topologies were evaluated in terms of their function in a UHF system for transcutaneous power transfer to an implanted device: planar dipole, meandered dipole, single-turn square loop, and three-turn square loop. These topologies were chosen for their relative ease of fabrication and their potential for use in thin, miniature implantable devices.

In the second part of this study, the power gain of transcutaneous systems was calculated with varying tissue characteristics for dipole and loop antenna systems. Maximum power gain for each configuration was compared to power gain with mismatch due to tissue variability. Optimizing matching networks for a particular tissue composition mimics designing a transcutaneous system based on the expected properties of the physiological implant location. Varying the tissue composition and tissue properties then represents variations that will be encountered using such a system in practice.

II. METHODS

Throughout this work, the power gains of transcutaneous systems were calculated from simulations in ANSYS HFSS 15.0, a 3-D electromagnetic field solver utilizing the finite element method. Each modeled system consisted of an external antenna and an implanted antenna separated by tissue, analyzed as a two-port network. Scattering parameters (S-parameters) obtained from simulation were used to calculate power gain with conjugate impedance matching and with impedance mismatch. Simulations were performed at 915 MHz to utilize the UHF ISM band for wireless communications and the sub-GHz range recommended for efficient midfield wireless power transfer to miniature implants [16]. The dimensions of the implant antenna in this work were constrained within 1 cm by 1 cm, and the antenna separations range from 3.5 mm to 16.1 mm. Therefore, the operating field regions in this work include both the reactive near field and radiative near field regions, and necessitate full-wave simulation [16], [21].

A. PART I: ANTENNA TOPOLOGIES AND DIMENSIONS

In the first part of this study, the simulated tissue was a simplified layered model consisting of skin, fat, and muscle, similar to that used in [16], [17], and [23]. The thickness of each layer was modeled with reference to values measured for the arm: 2.2 mm skin, 10.8 mm fat, and 35 mm muscle [10]. Tissue properties were defined according to measured values for skin, fat, and muscle [24]. For simulations in tissue, the antenna was positioned between the fat and muscle layers as it would be for a subcutaneous implant, as shown in Figure 1, resulting in an antenna separation of 13 mm [25].

Fabricated antennas were tested experimentally using tissue phantoms, and antenna parameters were measured using a vector network analyzer (VNA) (Agilent 8753ES S-Parameter Network Analyzer). Layered tissue phantoms were constructed according to procedures and formulations in [26] and [27], with layer dielectric properties similar to human skin, fat, and muscle, and layer thicknesses based on measured values for the arm (to match the simulation model). During measurements, the implanted antenna was positioned between the layers of fat and muscle phantom, to replicate the positioning of the implant in simulation.

1) ONE-PORT MODEL VERIFICATION

To first validate the simulation model, one-port simulations of implanted antennas were performed in the tissue model and in air and compared to one-port measurements on fabricated antennas. Initially examining only the implanted antenna decreased the simulation complexity and simplified the measurements necessary to verify the simulation model. Values of the input port reflection coefficient (S_{11}) were obtained from one-port simulations of the two simplest antenna topologies: a planar dipole and a single-turn loop, shown in Figure 1. The input port reflection coefficient is directly related to the input impedance of the antenna, which is a function of the antenna
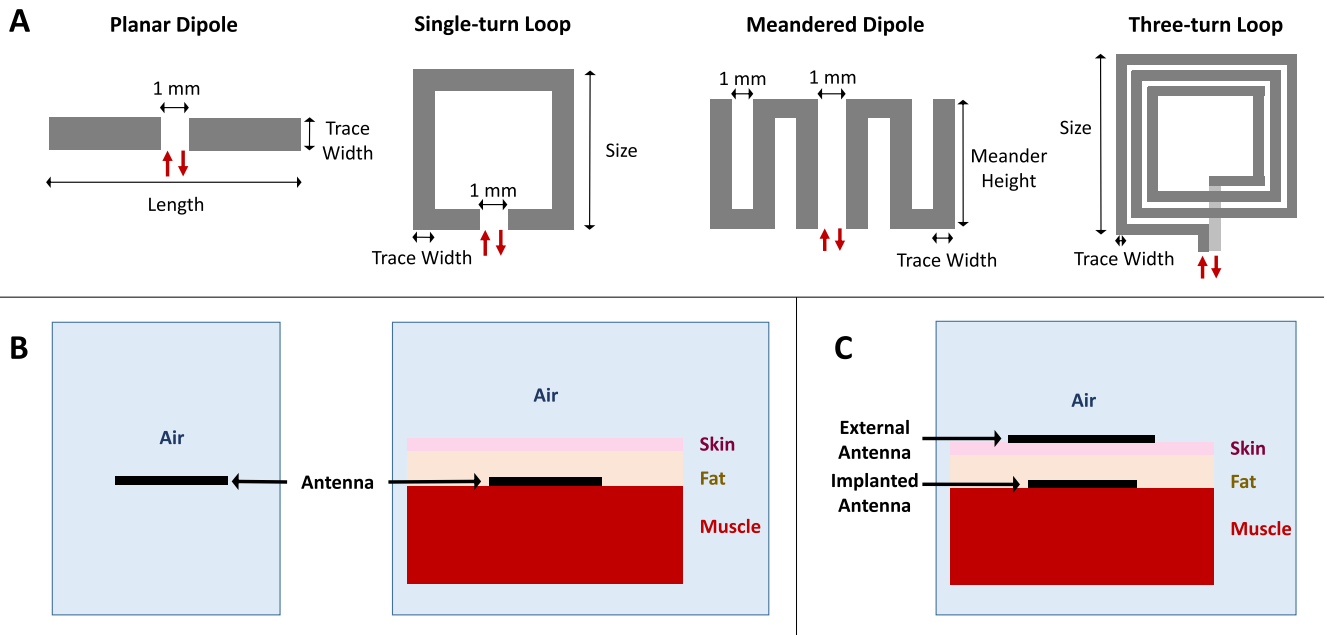
FIGURE 1. (A) Planar dipole, single-turn loop, meandered dipole, and three-turn loop antenna topologies used in simulation. (B) Model setup for one-port simulations and measurements, showing location of antenna in air and tissue. (C) Model setup for two-port simulations, showing location of external and implanted antennas in the tissue model.

size and topology and the surrounding media. Simulated and measured S_{11} were therefore used to evaluate the discrepancies between the simulation model and fabricated antennas of the same topology and dimensions.

A feed gap of 1 mm was chosen for both the dipoles and the loops, due to the dimensions of standard connectors that would be used later for measurements. The dipole length and trace width and the loop size and trace width (as labeled in Figure 1) were varied in simulation. The same sets of antenna dimensions were simulated in tissue and air to allow use of the same fabricated antennas for measurements in tissue and air. The simulated dimensions of the dipole and loop were chosen such that the dipole length and loop perimeter extended up to at least the first expected resonance in fat, with fat having the lowest permittivity and therefore longest wavelength. The dimensions were also set according to printed circuit board manufacturing specifications and to prevent any overlap of the traces. The increment size of the swept dimensions was chosen to observe trends in S_{11} over the full range of simulated dimensions, including the expected resonances in tissue (see Appendix A).

The simulated values of S_{11} were compared with VNA measurements of the fabricated antennas, using layered tissue phantoms [26], [27]. Each of the fabricated geometries corresponded to one of the simulated configurations. The fabricated geometries were chosen to compare trends observed with changing each dimension in simulation. The expected resonances were in agreement between simulation and measurement to within 2 cm dipole length and 1 cm loop size, with differences attributed to phantom dielectric properties (see Appendix A).

2) TWO-PORT ANTENNA SYSTEMS

Next, both implanted and external antennas were simulated with the tissue model as a two-antenna system and analyzed as a two-port network to compare the performance of each antenna topology. This was necessary as simulations of the implanted antenna alone do not adequately inform about the behavior of the antenna in a transcutaneous UHF system including both implanted and external antennas. The proximity of the implanted antenna in such a system affects the fields of the external antenna.

Two-antenna simulations were performed to evaluate systems of planar dipoles, meandered dipoles, single-turn loops, and three-turn loops as shown in Figure 1. The two-antenna simulations included an external antenna and an implanted antenna separated by layers of tissue, modeling transcutaneous power transfer to a subcutaneous implanted device. The antenna positions were as depicted in Figure 1: the implanted antenna was positioned under the layers of skin and fat and on top of a layer of muscle, while the external antenna was positioned on the external surface of the skin, such that the layers of skin and fat separated the two antennas.

The implanted and external antennas were of the same topology within each simulated two-antenna system. The dimensions of the antennas were varied in simulation to compare power gain across different configurations of implanted and external antenna dimensions. The feed gaps and trace widths of the antennas were chosen with the same rationale previously discussed for one-port simulations and measurements. A maximum size limit of 1 cm square was chosen for the implanted antenna, a size comparable to other works on implantable antennas with dimensions ranging from 1 mm
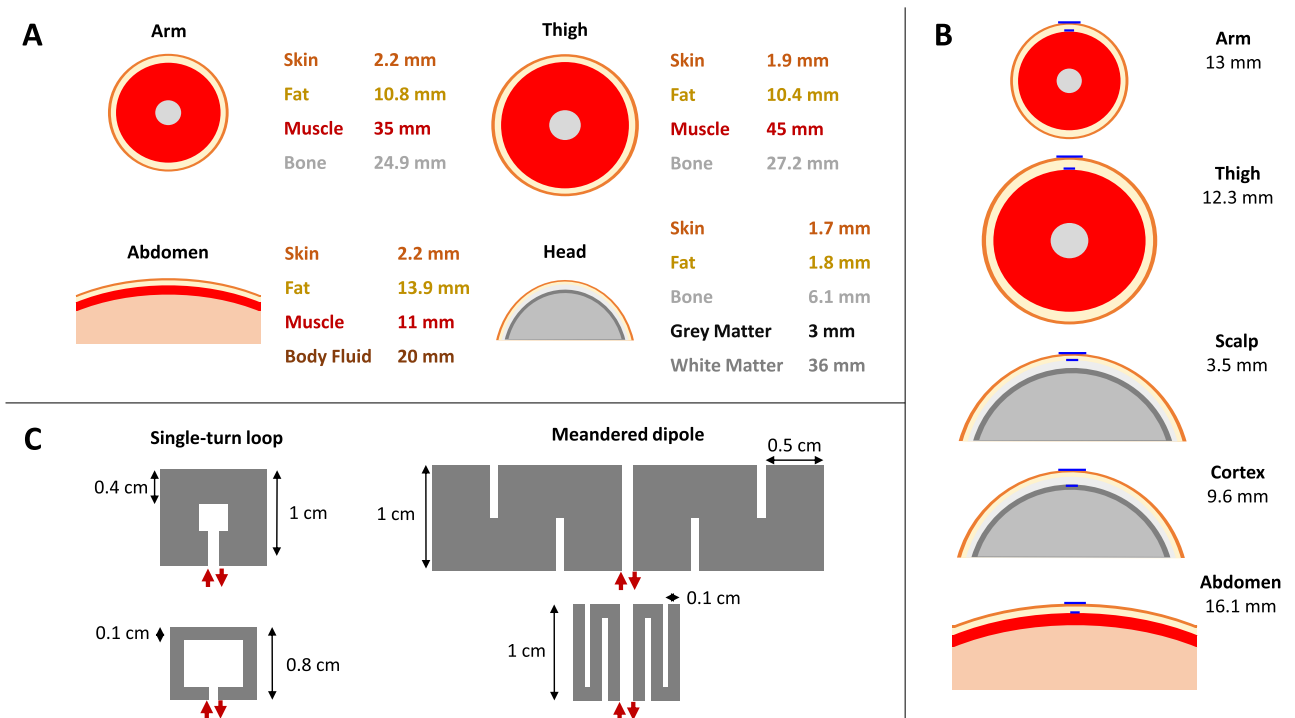
FIGURE 2. Tissue models of five different implantation locations and antenna topologies used in simulation: (A) Tissue layers and thicknesses at each location. (B) Implant locations: under skin and fat in the arm, thigh, abdomen, and head (scalp), under the skull in the head (cortex), with the indicated tissue thicknesses and antenna positioning. (C) Single-turn loop and meandered dipole antenna topologies. The dimensions of the antennas were chosen to achieve peak gain with an implanted antenna of size less than 1 cm by 1 cm and an external antenna of size less than approximately 3 cm by 3 cm.

by 1 mm to 3 cm by 2 cm [28]–[34]. The size constraints on an external antenna are more relaxed, but the transmitter size was kept under 3 cm square to constrain the number of simulation iterations. The tissue geometry and composition were held constant while the antenna dimensions were varied.

The following dimensions of each antenna topology were varied in simulation (as labeled in Figure 1): the meander height and trace width of the meander dipole, the loop size and trace width of the three-turn loop, the length and trace width of the planar dipole, and the loop size and trace width of the single-turn loop. The dimensions were swept in simulation within the previously stated size limits for the implant and the external antenna (see values in Appendix A).

The antennas were simulated at every combination of implant and external dimensions, such that a single implant size and trace width was simulated with each of the sizes and trace widths of the external antenna. This resulted in a total of 720 configurations of the planar dipole system, 360 configurations of the meandered dipole system, 360 configurations of the single-turn loop system, and 360 configurations of the three-turn loop system. More configurations were possible for the dipole due to the lack of restrictions on trace width that were necessary to prevent overlapping of traces in the meandered dipole and the loop topologies.

S-parameters were used to calculate maximum power gain for each system. The maximum power gain for each set of dimensions was calculated as the power gain assuming

simultaneous conjugate matching at the source and the load. The *peak power gain* was then determined as the greatest maximum power gain for a given topology across all of the combinations of external and implanted antenna dimensions. The peak gain represents the maximum power transfer between an external antenna of up to 3 cm square and a subcutaneous implant of up to 1 cm square, given a particular antenna topology and operating frequency.

As implementing a complete physical system requires realizable impedance matching networks, the impedance values required for conjugate matching were also considered when comparing antenna topologies.

B. PART II: TISSUE VARIABILITY
The tissue variability analysis was performed using single-turn square loops or meandered dipoles for the external and implanted antennas, based on the results of the first part of the study. The dimensions of the antennas, shown in Figure 2, were held constant to isolate the effects of changing the tissue characteristics.

The analysis was performed as follows: first, maximum power gain with simultaneous conjugate matching was calculated at one of five implant locations shown in Figure 2 (arm, thigh, scalp, cortex, or abdomen); next, the antenna system location was varied over the five locations with fixed matching networks, and the power gain at each location was calculated using the S-parameters from simulation and the impedances of the fixed matching networks.

The implant antenna was positioned under skin and fat in the arm, thigh, abdomen, and scalp locations, and under the skull in the cortex location (Figure 2). The external antenna was always positioned in contact with the external skin surface. For each configuration, power gain without conjugate matching was compared to maximum power gain achievable with simultaneous conjugate matching. The effect of changing tissue dielectric properties was also investigated by comparing the gain at each location with dry skin and wet skin, based on reported properties [24].

Tissue thicknesses and properties were varied to cover a range of tissue locations measured in the literature representing potential locations of transcutaneous systems. The tissue composition in the arm and thigh was simplified to layers of skin, fat, muscle, and bone. Tissue layers used to represent the abdomen were skin, fat, muscle, and body fluid. Tissue layers used for the head were skin, fat, skull, gray matter, and white matter. Tissue layer thicknesses were modeled according to measured values reported throughout the literature [8], [10], [35]–[39]. Dielectric properties of each tissue were defined according to reported values [24]. Each location and the associated tissue layer thicknesses are shown in Figure 2. The model of the abdomen included body fluid behind the muscle extended to terminate the model, to simulate the abdominal cavity. The model of the head included brain tissue behind the skull with white matter extended to terminate the model [40].
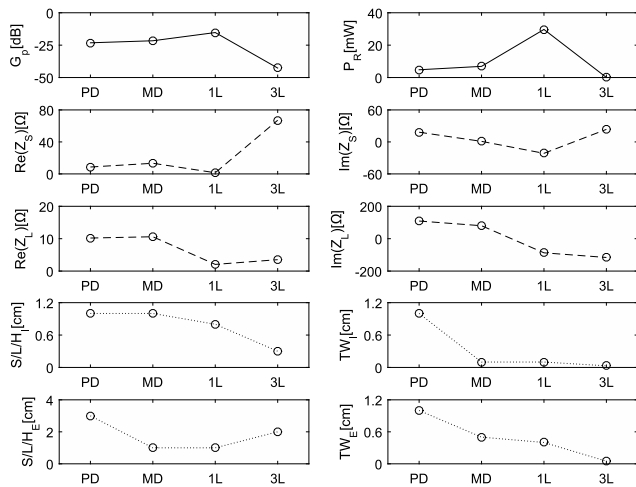

FIGURE 3. Peak power gains for each topology and associated antenna dimensions and impedances required for conjugate matching.
PD = planar dipole; MD = meandered dipole; 1L = single-turn loop; 3L = three-turn loop; G_P = peak power gain; P_R = power received at the implant with 1 W delivered at the source; Z_S, Z_L = impedance looking toward the source or load required for conjugate matching; S/L/H_I, S/L/H_E = implant (I) or external (E) loop size (S), dipole length (L), or meander height (H) that resulted in peak power gain; TW_I, TW_E = implant (I) or external (E) trace width (TW) that resulted in peak power gain.

III. RESULTS
A. PART I: ANTENNA TOPOLOGIES AND DIMENSIONS
The results of the antenna topology comparison are visually summarized in Figure 3. For the planar dipole, a peak power gain of −23.19 dB occurred at an implanted dipole length
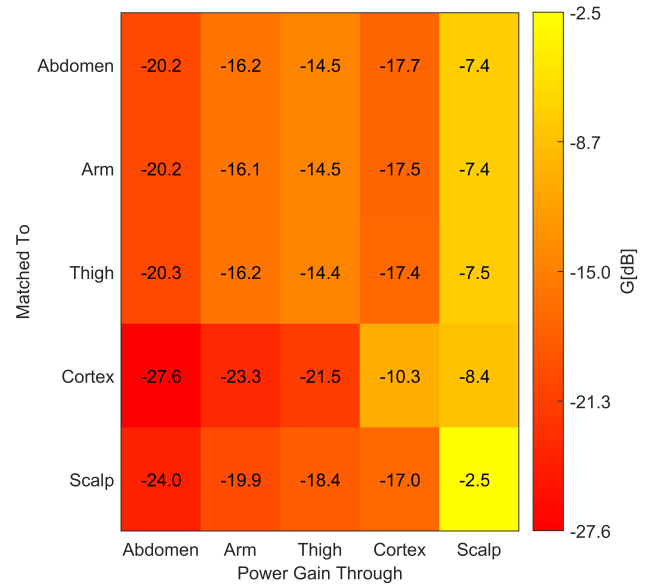

FIGURE 4. Power gain (G) of the single-turn loop system through each tissue location with matching networks optimized to each tissue location.
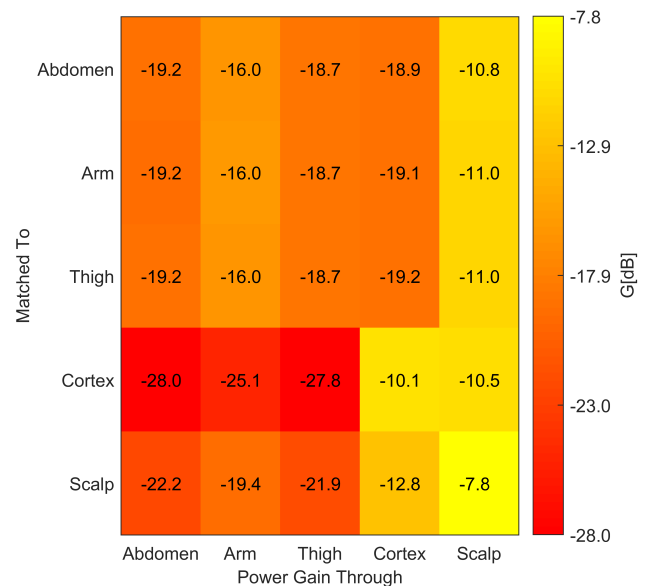

FIGURE 5. Power gain (G) of the meandered dipole system through each tissue location with matching networks optimized to each tissue location.

of 1 cm and trace width of 1 cm, and an external dipole length of 3 cm and trace width of 1 cm. For the meandered dipole, a peak power gain of −21.61 dB occurred at an implant meander height of 1 cm and trace width of 0.1 cm, and an external meander height of 1 cm and trace width of 0.5 cm.

For the single-turn loop, a peak power gain of −15.27 dB occurred at an implanted loop size of 0.8 cm and trace width of 0.1 cm, and external loop size 1 cm and trace width of 0.4 cm. The implant loop size at the point of peak power gain was slightly smaller than external, such that the loop trace was aligned along the center of the wider external
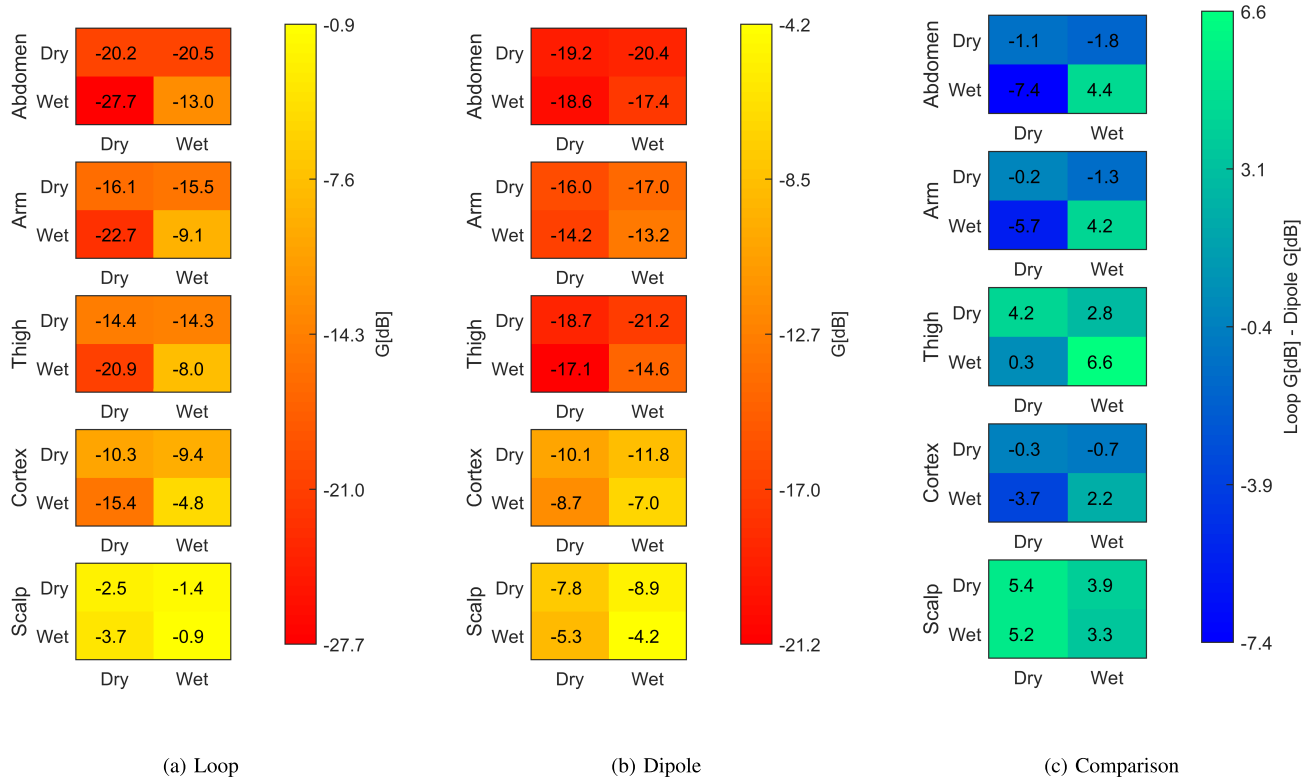
FIGURE 6. Power gain (G) of (a) the loop system, (b) dipole system, and (c) gain difference between the loop and dipole systems, through wet skin or dry skin with matching networks optimized to wet skin or dry skin at each tissue location. Vertical axes indicate the tissue that matching networks were optimized to; Horizontal axes indicate the tissue through which power gain was calculated.

loop trace. For the three-turn loop, a peak power gain of −42.68 dB occurred at an implant loop size of 0.3 cm and trace width of 0.03 cm, and external loop size of 2 cm and trace width of 0.05 cm.

Assuming a power of 1 W delivered at the source, the results imply a peak received power of 29.7 mW for single-turn loops, 4.8 mW and 6.9 mW for planar dipoles and meandered dipoles, respectively, and 53.9 μW for three-turn loops. This obviously does not account for absorption limitations and assumes a fixed operating frequency, and therefore primarily indicates how the topologies compare in terms of peak power gain and trends associated with changing dimensions.

The maximum power gain of the planar dipole increased with greater length and trace width of the external and implanted dipole. The power gain of the meandered dipole system was greatest when the external and internal dipole meander heights were equal. The power gain increased with greater trace width of both the external and implanted dipole. The meandered dipole length was a function of the trace width, so this result is analogous to the planar dipole system.

The power gain of the single-turn loop system was greatest for loops of approximately the same size, and increased with greater trace width of both the implanted and external loops. Power gain of the three-turn loop system increased with greater trace width of both the external and internal loops,

and was greatest for the smallest implanted loop size and an external loop size of 2 cm (see Appendix A for more details on the results of Part I).

B. PART II: TISSUE VARIABILITY
The results of the tissue variability analysis are summarized in Figures 4, 5, 6a, and 6b. For both antenna systems, the highest maximum gains were possible through the scalp, and the lowest maximum gains occurred through the abdomen. For the single-turn loop system, there was a consistent trend of decreased maximum gain with increased implantation depth. For the meandered dipole system, the greatest power gains occurred through the scalp, followed by the cortex, arm, thigh, and abdomen. This corresponds to decreased gain with increased depth except for the arm and thigh. The meandered dipole was determined to be more affected than the single-turn loop by differences in the tissue geometry. This is a potential explanation for the lack of a consistent trend of decreased gain with increased depth for the dipole system.

A comparison of the loop and dipole power gain in each configuration is shown in Figure 7 and Figure 6c. The loop antenna system afforded higher maximum gain than the dipole system through all but the thickest tissue (abdomen), consistent with loop antennas being most effective in the near field and the observation that magnetic field strength decreases with greater separation of the loop antennas [12].
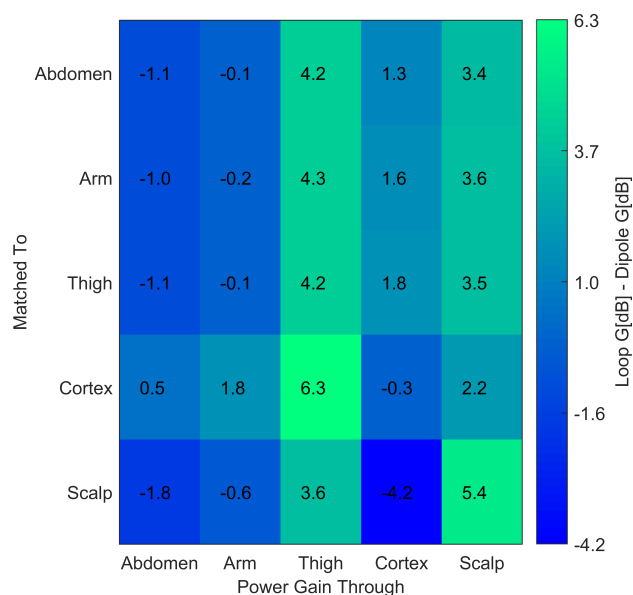
FIGURE 7. Gain difference between the loop and dipole systems through each tissue location.

From the first part of this study, it was determined that increasing the size of the external loop antenna at this separation did not improve the gain, while increasing the length of the external dipole increased the gain for the same size of implanted antenna. Therefore, the dipole system presents an advantage for greater implantation depth. It is expected that further increase in the external dipole length could allow greater implant depths, within safety limitations on tissue absorption.

The gain of the loop system varied over a wider range than the dipole system when the tissue location was varied. The power gain of the dipole system was therefore more consistent through variable tissue, but was generally lower than the loop system. Similar to the results across body locations, the loop system generally provided higher gains while the dipole system provided greater consistency in the presence of dielectric property variations.

The lowest gains with non-optimal matching networks through the abdomen, arm, thigh, and scalp were seen when the matching was optimized to the cortex location. Conversely, when matching was optimized to the abdomen, arm, or thigh, the gains through the arm and thigh were greater than the gain at the cortical location even though the implantation depth is less at the cortex. These effects can be attributed to the difference in tissue composition: at the abdomen, arm, and thigh locations there were layers of skin and fat between the antennas, while at the cortex location there were layers of skin, fat, and bone.

At the greater loop separation in the abdomen, the power gain was more sensitive to changes in tissue properties, indicating that at greater implantation depths the power transfer of the loop system was not solely dependent on the magnetic field. With the dipole system, there was not a trend

of increased gain sensitivity to tissue dielectric property variations with implantation depth. In fact, gain was most consistent through the abdomen, the location with the lowest achievable gain with optimal matching.

For both antenna systems, higher gains were possible through wet skin, presumably due to higher permittivity of wet skin and therefore electrically larger antennas. However, the gain was more sensitive to changes in properties when matching was optimized for wet skin, likely due to a combination of mismatch and electrically smaller antennas in dry skin.

IV. DISCUSSION

Tissue variability is an important consideration for robust implantable medical devices utilizing transcutaneous power. Tissue structure and properties have been documented to vary among patients, across locations of the body, and over time [7]–[11]. The results of this study indicate that power gain is highly dependent on the antenna topology and impedance matching, including impedance mismatch due to tissue variations, and maximum power gain for a given system is determined by implantation depth, antenna size, and tissue characteristics.

For the initial antenna simulations using a planar tissue model and tissue thicknesses representing the arm, the single-turn loop showed the greatest peak power gain. However, the small real impedances required for conjugate matching could prove difficult to achieve with matching networks in a physical system. The dipole topologies offered greater real impedances for matching. Comparing the dipole topologies, the meandered dipole showed higher peak gain than the planar dipole, with similar impedances required for matching. The multiple-turn loop provided even higher impedances for conjugate matching, however the maximum achievable gain was orders of magnitude less than that of the other topologies.

In applications where the size of the external antenna is not constrained, these results show that greater power gain can be achieved for the dipole systems by increasing the external dipole length beyond the length of the implanted dipole. In the loop systems investigated in this work, further increasing the size of the external loop antenna did not afford increased power gain. Additionally, increasing the width of the planar dipole increased the power gain of the system, while increasing the meander height of the meandered dipole did not improve the gain. For an application with unconstrained external antenna dimensions, the planar dipole topology affords the greatest peak power gain for a fixed implant size. Further work includes determining the achievable power delivery within constraints on energy absorption in tissue.

The performance of each antenna topology can be explained by examining the fields of each system [41], [42]. For example, the greatest power gain for the loop systems was achieved when the magnetic field vectors were most perpendicular to the plane of the implant loop, consistent with power transfer in loop systems occurring primarily through inductive coupling. The increase in gain with both dipole

length and width indicate combined radiative and reactive mechanisms of power transfer. The dipole antennas in this work couple capacitively due to their proximity, and the meandered dipoles achieve power transfer through a combination of capacitive and inductive coupling [42]. Other works have used dipoles in similar proximity, referring to the antenna systems as electrodes due to the coupling method of power transfer [19].

Optimizing to achieve maximum power gain through a particular tissue composition is a reasonable starting point for designing a transcutaneous system, but in practice the system will encounter variable tissue configurations that will affect the power delivered. Ideally, an adaptive system would be implemented to adjust the matching network to each tissue configuration, although the power gain of even an adaptive system will be subject to limits related to implantation depth and tissue characteristics [22]. Additionally, the power limitations of passive implantable devices may limit adaptive matching at the implant. It is therefore important to quantify the effects of non-optimal impedance matching due to expected environmental variations, as explored in this study.

In this study, antenna dimensions were optimized using one tissue model, and then applied to various tissue configurations to examine effects of tissue variability. The topologies used in the current study were chosen to be representative of power transfer through capacitive or inductive coupling, and the effects of tissue variability are expected to be similar for antennas utilizing similar power transfer mechanisms in the near- and mid-field.

The choice of antenna topology based on power gain through a fixed tissue structure presents its own issues in that the chosen topology may not present the same power gain advantages through another tissue configuration. That is, the choice of antenna topology (and dimensions) can be biased by the choice of tissue structure to design and evaluate potential topologies. In this work, although the loop antenna system showed the highest peak gain in the first part of the study, the meandered dipole system showed similar or higher gain for some tissue configurations and impedance mismatch. In particular, the dipole system surpassed the gain of loop antenna system for larger antenna separations. Therefore, quantifying the effects of tissue variability is not only important for a system to operate despite tissue variability among patients and over time, but also to account for differences between the design environment and the environment in practice.

In this study, changes in tissue properties and composition caused the greatest mismatch losses, while tissue thickness and geometry determined the maximum achievable gain. The gain with mismatch is expected to be lower through a given tissue composition if the matching networks have not been optimized to a similar tissue composition, as evidenced by the lower gains through subcutaneous locations when matching networks were optimized for a cortical implant. Shallow implantation depth and higher permittivity present favorable conditions for power transfer due to limited attenuation and larger electrical size of the antennas, although the results of

this study suggest that designing matching networks for these conditions will lead to the system gain being more sensitive to environmental variations in practice.

Based on the tissue variability analysis in this work, the antenna topology and matching networks can be designed to achieve more consistency across tissues (with lower gain) or higher gain through certain tissues (with more gain variability), depending on the power transfer mechanisms. This is analogous to designing a wide- or narrow-band antenna. For example, if a device is expected to be used at several body locations with different tissue compositions, and particularly through thicker tissue such as the abdomen, a dipole system is more desirable. If power delivery is to be maximized and the implantation depth is comparable to the size of the antennas, a loop antenna system is likely to be more effective.

Variations in gain due to frequency are expected to be similar to the variations in gain due to changes in tissue properties, because both frequency and tissue properties affect antenna electrical size and wavelength within the tissue. The meandered dipole is a more wideband antenna than the loop, and therefore expected to be less affected by changes in frequency as it is less affected by changes in tissue properties [42].

V. CONCLUSION

This study investigated the effects of varying tissue structure and properties in wireless transcutaneous systems, by evaluating maximum power gain and power gain with impedance mismatch. Four antenna topologies were first evaluated in terms of peak power gain through a given tissue configuration based on measured tissues in the arm, over a range of external and implanted antenna dimensions. A single-turn loop and a meandered dipole system were then evaluated with varying tissue structure representing different locations on the body, and varying tissue properties representing fluctuations in tissue water content. The results indicate that a single-turn loop antenna topology provides the highest peak gain with the smallest implanted antenna, while dipole systems provide higher real impedance for conjugate matching and the ability to increase gain with a larger external antenna. At close antenna separations, the loop system was shown to provide higher power gain than the meandered dipole system. At antenna separations greater than the loop dimensions, the dipole system achieved higher gain, and the power gain of the dipole system was overall less sensitive to changes in tissue structure and properties. The results suggest that through choices of matching networks and antenna topologies, a system can be designed to maximize peak power gain for a narrow range of tissue properties, or to achieve greater consistency with lower peak power gain through variable tissue.

APPENDIX A
ANTENNA SIMULATION AND MEASUREMENTS

In simulation in air, a minimum S_{11} of -20.9 dB occurred at a dipole length of 13.5 cm and trace width of 0.1 cm. In simulation in tissue, a minimum S_{11} of -13.4 dB occurred at a dipole

length of 6 cm and a trace width of 0.1 cm. The first resonance of a dipole is expected to occur at 0.47 wavelengths [41]. The wavelength in fat at 915 MHz is approximately 14 cm, so the resonance was expected at a dipole length of 6.6 cm. The wavelength in air at 915 MHz is approximately 33 cm, so the resonance was expected at a dipole length of 15.5 cm. The resonant length decreases as the dipole width increases, which explains the smaller resonant length in both air and tissue [41]. The measured S_{11} in air showed a difference of up to 2.79 dB around the resonance point, but the resonance occurred at approximately the same dipole length as in simulation. Otherwise the measurements agreed with the simulated values to within 1 dB. The resonance points were shifted in tissue, indicating that the wavelength in the fat phantom was longer than the wavelength in the simulated fat layer, therefore the associated phantom permittivity was lower than the permittivity used in simulation. The resonance in measurement and simulation occurred within 2 cm of dipole length (Figure 8).
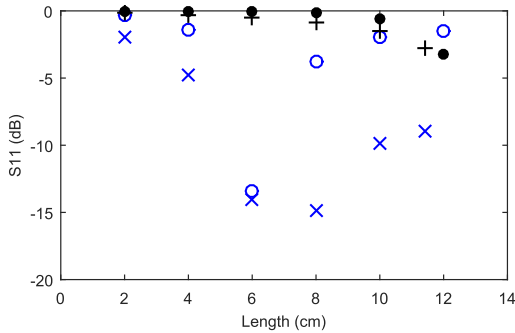

FIGURE 8. Reflection coefficient (S_{11}) of dipole antennas in air (Simulated: ● and Measured: +) and in tissue (Simulated: ○ and Measured: ×).

In simulation in air, a minimum S_{11} of −9.86 dB occurred at a loop size of 7 cm and trace width of 0.01 cm. Because 7 cm was the maximum simulated loop size, the minimum does not represent the resonance point, but was used as a reference for experimental comparisons. In simulation in tissue, a minimum S_{11} of −33.4 dB occurred at a loop size of 4 cm and trace width of 0.3 cm. The first resonance of a loop is expected to occur at a circumference of 1.2 wavelengths [41], so the resonance was expected at a loop size of approximately 4.2 cm in tissue and 9.9 cm in air. The measurements for the loop in air agreed with simulation results to within 2 dB. The resonance in simulation and measurement occurred within 1 cm loop size, although loop S_{11} in simulation was considerably lower than measured (Figure 9).

Antenna dimensions used in one-port simulations are listed in Table 1. Antenna dimensions used in two-port simulations are listed in Table 2.

APPENDIX B
POWER GAIN CALCULATION
The equations below were used to calculate power gain assuming simultaneous conjugate matching, where S_{11}, S_{21},
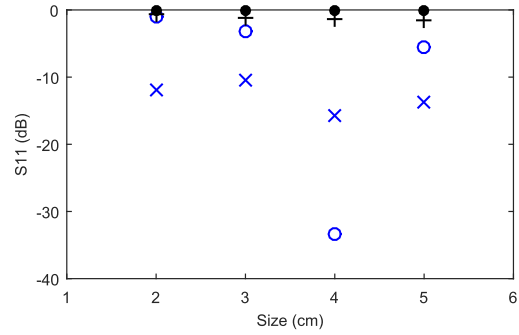

FIGURE 9. Reflection coefficient (S_{11}) of loop antennas in air (Simulated: ● and Measured: +) and in tissue (Simulated: ○ and Measured: ×).

TABLE 1. Planar dipole and single-turn loop dimensions (cm) for one-port simulations in air and in tissue.

Dimension	Range	Increment
Planar Dipole		
Length	0.5 - 14	0.5
Trace Width	0.1 - 1	0.1
Single-turn Loop		
Size	1.5 - 7	0.5
Trace Width	0.01 - 0.5	0.02 (<0.2), 0.1 (>0.2)

TABLE 2. Simulated dimensions (cm) of the external and implanted antenna of each topology in two-antenna simulations.

Dimension	Implant Range	Increment	External Values
Planar Dipole			
Length	0.3 - 1.0	0.1	1.0, 2.0, 3.0
Trace Width	0.1 - 1.0	0.1	0.1, 0.5, 1.0
Meandered Dipole			
Length	0.62 - 1.10	0.12	1.1, 2.3, 3.5
Meander Height	0.3 - 1.0	0.1	1.0, 2.0, 3.0
Single-turn Loop			
Size	0.3 - 1.0	0.1	1.0, 2.0, 3.0
Trace Width	0.02 - 0.10	0.02	0.1, 0.3, 0.4
Three-turn Loop			
Size	0.3 - 1.0	0.1	1.0, 2.0, 3.0
Trace Width	0.01 - 0.03	0.005	0.01, 0.03, 0.05

S_{12}, and S_{22} are the S-parameters from simulation [43]. Equation 1 represents maximum power gain (G_{max}) with simultaneous conjugate matching at the source and load, where Γ_S is the reflection coefficient looking toward the source and Γ_L is the reflection coefficient looking toward the load. Equation 2 represents the reflection coefficient looking toward the source required for simultaneous conjugate matching, where B_1 and C_1 are defined by Equations 4 and 6, respectively. Equation 3 represents the reflection coefficient looking toward the load required for simultaneous conjugate

matching, where B_2 and C_2 are defined by Equations 5 and 7, respectively. The value Δ in Equations 4, 5, 6, and 7 is defined by Equation 8 [43].

$$G_{max} = \frac{1}{1 - |\Gamma_S|^2} |S_{21}|^2 \frac{1 - |\Gamma_L|^2}{|1 - S_{22}\Gamma_L|^2} \tag{1}$$

$$\Gamma_S = \frac{B_1 \pm \sqrt{B_1^2 - 4|C_1|^2}}{2C_1} \tag{2}$$

$$\Gamma_L = \frac{B_2 \pm \sqrt{B_2^2 - 4|C_2|^2}}{2C_2} \tag{3}$$

$$B_1 = 1 + |S_{11}|^2 - |S_{22}|^2 - |\Delta|^2 \tag{4}$$

$$B_2 = 1 + |S_{22}|^2 - |S_{11}|^2 - |\Delta|^2 \tag{5}$$

$$C_1 = S_{11} - \Delta S_{22}^* \tag{6}$$

$$C_2 = S_{22} - \Delta S_{11}^* \tag{7}$$

$$\Delta = S_{11}S_{22} - S_{12}S_{21} \tag{8}$$

ACKNOWLEDGMENT

REFERENCES

[1] V. Chawla and D. S. Ha, "An overview of passive RFID," *IEEE Commun. Mag.*, vol. 45, no. 9, pp. 11–17, Sep. 2007.

[2] D. Halperin, T. Kohno, T. S. Heydt-Benjamin, K. Fu, and W. H. Maisel, "Security and privacy for implantable medical devices," *IEEE Pervasive Comput.*, vol. 7, no. 1, pp. 30–39, Jan./Mar. 2008.

[3] M. Rasouli and L. S. J. Phee, "Energy sources and their development for application in medical devices," *Expert Rev. Med. Devices*, vol. 7, no. 5, pp. 693–709, 2010.

[4] J. E. Ferguson and A. D. Redish, "Wireless communication with implanted medical devices using the conductive properties of the body," *Expert Rev. Med. Devices*, vol. 8, no. 4, pp. 427–433, 2011.

[5] J. Olivo, S. Carrara, and G. D. Micheli, "Optimal frequencies for inductive powering of fully implantable biosensors for chronic and elderly patients," in *Proc. IEEE SENSORS*, Nov. 2010, pp. 99–103.

[6] J. Olivo, S. Carrara, and G. De Micheli, "Energy harvesting and remote powering for implantable biosensors," *IEEE Sensors J.*, vol. 11, no. 7, pp. 1573–1586, Jul. 2011.

[7] C. Gabriel, S. Gabriel, and E. Corthout, "The dielectric properties of biological tissues: I. Literature survey," *Phys. Med. Biol.*, vol. 41, no. 11, pp. 2231–2249, Nov. 1996.

[8] H. Kanehisa, M. Miyatani, K. Azuma, S. Kuno, and T. Fukunaga, "Influences of age and sex on abdominal muscle and subcutaneous fat thickness," *Eur. J. Appl. Physiol.*, vol. 91, nos. 5–6, pp. 534–537, 2004.

[9] A. Peyman, C. Gabriel, E. H. Grant, G. Vermeeren, and L. Martens, "Variation of the dielectric properties of tissues with age: The effect on the values of SAR in children when exposed to walkie–talkie devices," *Phys. Med. Biol.*, vol. 54, no. 2, pp. 227–241, 2009.

[10] M. A. Gibney, C. H. Arce, K. J. Byron, and L. J. Hirsch, "Skin and subcutaneous adipose layer thickness in adults with diabetes at sites used for insulin injections: Implications for needle length recommendations," *Current Med. Res. Opinion*, vol. 26, no. 6, pp. 1519–1530, 2010.

[11] J. Schumacher, A. Engelke, K. F. Wagner, W. Eichler, U. Markert, and K. F. Klotz, "Measurement of peripheral tissue thickness by ultrasound during the perioperative period," *Brit. J. Anaesthesia*, vol. 82, no. 4, pp. 641–643, 1999.

[12] G. Marrocco, "RFID Antennas for the UHF remote monitoring of human subjects," *IEEE Trans. Antennas Propag.*, vol. 55, no. 6, pp. 1862–1870, Jun. 2007.

[13] A. Alomainy, Y. Hao, and D. M. Davenport, "Parametric study of wearable antennas with varying distances from the body and different on-body positions," in *Proc. IET Seminar Antennas Propag. Body-Centric Wireless Commun.*, 2007, pp. 84–89.

[14] T. Dissanayake, K. P. Esselle, and M. R. Yuce, "Dielectric loaded impedance matching for wideband implanted antennas," *IEEE Trans. Microw. Theory Techn.*, vol. 57, no. 10, pp. 2480–2487, Oct. 2009.

[15] J. Kim and Y. Rahmat-Samii, "Planar inverted-F antennas on implantable medical devices: Meandered type versus spiral type," *Microw. Opt. Technol. Lett.*, vol. 48, no. 3, pp. 567–572, 2006.

[16] A. S. Y. Poon, S. O'Driscoll, and T. H. Meng, "Optimal frequency for wireless power transmission into dispersive tissue," *IEEE Trans. Antennas Propag.*, vol. 58, no. 5, pp. 1739–1750, May 2010.

[17] M. Mark *et al.*, "Wireless channel characterization for mm-size neural implants," in *Proc. Annu. Int. Conf. IEEE Eng. Med. Biol. Soc.*, Aug. 2010, pp. 1565–1568.

[18] X. Liu, "Design, optimization and implementation of an Ortho-tag RFID system," Ph.D. dissertation, Dept. Elect. Comput. Eng., Univ. Pittsburgh, Pittsburgh, PA, USA, 2011.

[19] X. Liu, J. L. Berger, A. Ogirala, and M. H. Mickle, "A touch probe method of operating an implantable RFID tag for orthopedic implant identification," *IEEE Trans. Biomed. Circuits Syst.*, vol. 7, no. 3, pp. 236–242, Jun. 2013.

[20] K. Bocan and E. Sejdić, "Transmission mechanisms with variable tissue properties in a paired electrode system for transcutaneous power," in *Proc. IEEE Int. Symp. Circuits Syst. (ISCAS)*, May 2016, pp. 2739–2742.

[21] *IEEE Standard for Safety Levels With Respect to Human Exposure to Radio Frequency Electromagnetic Fields, 3 kHz to 300 GHz*, IEEE Standard C95.1-2005, 2005.

[22] K. N. Bocan and E. Sejdić, "Adaptive transcutaneous power transfer to implantable devices: A state of the art review," *Sensors*, vol. 16, no. 3, p. 393, 2016.

[23] A. Drossos, V. Santomaa, and N. Kuster, "The dependence of electromagnetic energy absorption upon human head tissue composition in the frequency range of 300–3000 MHz," *IEEE Trans. Microw. Theory Techn.*, vol. 48, no. 11, pp. 1988–1995, Nov. 2000.

[24] S. Gabriely, R. Lau, and C. Gabriel, "The dielectric properties of biological tissues: II. Measurements in the frequency range 10 Hz to 20 GHz," *Phys. Med. Biol.*, vol. 41, no. 11, pp. 2251–2269, 1996.

[25] S. A. Hacking, J. D. Bobyn, K. Toh, M. Tanzer, and J. J. Krygier, "Fibrous tissue ingrowth and attachment to porous tantalum," *J. Biomed. Mater. Res.*, vol. 52, no. 4, pp. 631–638, 2000.

[26] E. Porter, J. Fakhoury, R. Oprisor, M. Coates, and M. Popović, "Improved tissue phantoms for experimental validation of microwave breast cancer detection," in *Proc. 4th Eur. Conf. Antennas Propag.*, Apr. 2010, pp. 1–5.

[27] M. Lazebnik, E. L. Madsen, G. R. Frank, and S. C. Hagness, "Tissue-mimicking phantom materials for narrowband and ultrawideband microwave applications," *Phys. Med. Biol.*, vol. 50, no. 18, pp. 4245–4258, 2005.

[28] U.-M. Jow and M. Ghovanloo, "Modeling and optimization of printed spiral coils in air, saline, and muscle tissue environments," *IEEE Trans. Biomed. Circuits Syst.*, vol. 3, no. 5, pp. 339–347, Oct. 2009.

[29] J. S. Ho *et al.*, "Wireless power transfer to deep-tissue microimplants," *Proc. Nat. Acad. Sci. USA*, vol. 11, no. 22, pp. 7974–7979, 2014.

[30] J. Kim and Y. Rahmat-Samii, "Implanted antennas inside a human body: Simulations, designs, and characterizations," *IEEE Trans. Microw. Theory Techn.*, vol. 52, no. 8, pp. 1934–1943, Aug. 2004.

[31] W. Li, D. C. Rodger, E. Meng, J. D. Weiland, M. S. Humayun, and Y.-C. Tai, "Flexible parylene packaged intraocular coil for retinal prostheses," in *Proc. Int. Conf. Microtechnol. Med. Biol.*, May 2006, pp. 105–108.

[32] S. Kim, P. Tathireddy, R. A. Normann, and F. Solzbacher, "Thermal impact of an active 3-D microelectrode array implanted in the brain," *IEEE Trans. Neural Syst. Rehabil. Eng.*, vol. 15, no. 4, pp. 493–501, Dec. 2007.

[33] J. S. Ho, S. Kim, and A. S. Y. Poon, "Midfield wireless powering for implantable systems," *Proc. IEEE*, vol. 101, no. 6, pp. 1369–1378, Jun. 2013.

[34] J. M. Rabaey *et al.*, "Powering and communicating with mm-size implants," in *Proc. Design, Autom. Test Eur. Conf. Exhibit.*, Mar. 2011, pp. 1–6.

[35] S. R. Garfin, M. J. Botte, R. S. Centeno, and V. L. Nickel, "Osteology of the skull as it affects halo pin placement," *Spine*, vol. 10, no. 8, pp. 696–698, 1985.

[36] M. Krotkiewski, A. Aniansson, G. Grimby, P. Björntorp, and L. Sjöström, "The effect of unilateral isokinetic strength training on local adipose and muscle tissue morphology, thickness, and enzymes," *Eur. J. Appl. Physiol. Occupat. Physiol.*, vol. 42, no. 4, pp. 271–281, 1979.

[37] A. R. Frisancho, "Triceps skin fold and upper arm muscle size norms for assessment of nutritional status," *Amer. J. Clin. Nutrition*, vol. 27, no. 10, pp. 1052–1058, 1974.

[38] H. Haapasalo, H. Sievanen, P. Kannus, A. Heinonen, P. Oja, and I. Vuori, "Dimensions and estimated mechanical characteristics of the humerus after long-term tennis loading," *J. Bone Mineral Res.*, vol. 11, no. 6, pp. 864–872, 1996.

[39] B. Mahaisavariya, K. Sitthiseripratip, T. Tongdee, E. L. J. Bohez, J. V. Sloten, and P. Oris, "Morphological study of the proximal femur: A new method of geometrical assessment using 3-dimensional reverse engineering," *Med. Eng. Phys.*, vol. 24, no. 9, pp. 617–622, 2002.

[40] K. L. Narr *et al.*, "Relationships between IQ and regional cortical gray matter thickness in healthy adults," *Cerebral Cortex*, vol. 17, no. 9, pp. 2163–2171, 2007.

[41] C. A. Balanis, *Antenna Theory: Analysis and Design*. Hoboken, NJ, USA: Wiley, 2005.

[42] D. M. Dobkin, *The RF in RFID: Passive UHF RFID in Practice*. Burlington, VT, USA: Newnes, 2007.

[43] D. M. Pozar, *Microwave Engineering*, 3rd ed. Hoboken, NJ, USA: Wiley, 2005.

KARA N. BOCAN (S'10) received the B.S. degree in electrical engineering and bioengineering from the University of Pittsburgh, Pittsburgh, PA, USA, in 2012, where she is currently pursuing the Ph.D. degree in electrical engineering.

Her research interests include tissue electromagnetics and adaptive tuning for wireless implantable medical devices.

MARLIN H. MICKLE (M'62–SM'86–F'96–LF'02) received the B.S.E.E., M.S.E.E., and Ph.D. degrees from the University of Pittsburgh, in 1961, 1963, and 1967, respectively. He was a Professor Emeritus with the Department of Electrical and Computer Engineering, University of Pittsburgh. Previously, he was the Bell of Pennsylvania/Bell Atlantic Professor and before that, the Nickolas A. DeCecco Professor with the School of Engineering, University of Pittsburgh. He held appointments as a Professor of electrical and computer engineering (primary), a Professor of computer engineering, a Professor of biomedical engineering, a Professor of industrial engineering, and a Professor of telecommunications. He was an Executive Director of the RFID Center of Excellence. He was the co-author and co-editor of over 20 books. In addition, he has authored or co-authored over 200 publications in refereed journals, conference proceedings, and so on. He holds over 40 patents, including a magnetically levitated gyro, a gyro optical sensor, energy harvesting, and antennas on a CMOS chip.

He was a recipient of the 1988 Recipient of the Systems Research and Cybernetics Award from the International Institute for Advanced Studies in Systems Research and Cybernetics, the Carnegie Science Center Award for Excellence in Corporate Innovation, in 2005, the University 225th Anniversary Medallion Award, the Ted Williams Award from Association for Automatic Identification and Mobility 2011; the Pitt Innovation Award, 2005, 2006, 2007, 2008, 2009, 2010, 2011, and 2012. Faculty Honor Roll 2001, Honorable Mention 2004 Carnegie Science Center Award, with Mary Besterfield Sacre, Bopaya Bidanda, Michael R. Lovell, Larry Shuman and Rakibar Chaterjee (Katz). He was active in the areas of energy harvesting and high technology RF medical and sensor applications. Seven spin-off companies have resulted from the University licensing of patents on which he is an inventor, including one that won the Best of Show for Emerging Technologies at the Consumer Electronics Show in Las Vegas, 2007, the Gold Level Winner Best of Sensors expo 2009, and the Design News Best New Products Award 2011.

ERVIN SEJDIĆ (S'00–GS'05–M'07–SM'16) received the B.E.Sc. and Ph.D. degrees in electrical engineering from the University of Western Ontario, London, ON, Canada, in 2002 and 2008, respectively.

He was a Post-Doctoral Fellow with the Holland Bloorview Kids Rehabilitation Hospital/University of Toronto and a Research Fellow in medicine with the Beth Israel Deaconess Medical Center/Harvard Medical School. He is currently an Associate Professor with the Department of Electrical and Computer Engineering, Swanson School of Engineering, the Department of Bioengineering, Swanson School of Engineering, the Department of Biomedical Informatics, School of Medicine, and the Intelligent Systems Program, Kenneth P. Dietrich School of Arts and Sciences, with the University of Pittsburgh, Pittsburgh, PA, USA. His research interests include biomedical and theoretical signal processing, swallowing difficulties, gait and balance, assistive technologies, rehabilitation engineering, anticipatory medical devices, and advanced information systems in medicine.

Dr. Sejdić received prestigious research scholarships from the Natural Sciences and Engineering Research Council of Canada in 2003 and 2005. He also received the Melvin First Young Investigators Award from the Institute for Aging Research at Hebrew Senior Life in Boston, MA, USA. In 2016, President Obama named Dr. Sejdić as a recipient of the Presidential Early Career Award for Scientists and Engineers, the highest honor bestowed by the United States Government on science and engineering professionals in the early stages of their independent research careers. In 2017, he was awarded the National Science Foundation CAREER Award, which is the National Science Foundation's most prestigious awards in support of the career-development activities of those scholars who most effectively integrate research and education within the context of the mission of their organization.

● ● ●